Colloids and Surfaces A: Physicochemical and Engineering Aspects 674 (2023) 131986

Contents lists available at ScienceDirect

Colloids and Surfaces A: Physicochemical and Engineering Aspects

journal homepage: www.elsevier.com/locate/colsurfa

Modeling inkjet dots from drop spreading, absorption and evaporation – An engineering approach

Carina Waldner [a,b], Alfons Ritzer [b,c], Ulrich Hirn [a,b,*]

[a] Institute of Bioproducts and Paper Technology, Graz University of Technology, Inffeldgasse 23, 8010 Graz, Austria
[b] CD Laboratory for Fiber Swelling and Paper Performance, Inffeldgasse 23, 8010 Graz, Austria
[c] Canon Production Printing Germany GmbH & Co KG, Siemensallee 2, 85586 Poing, Germany

HIGHLIGHTS

- Evaluation of inkjet printed dots of 140 uncoated paper-liquid pairings.
- Substrates and liquids were tailored to cover operation window of an inkjet printer.
- Inkjet printed dot area is simulated from spreading, absorption and evaporation.
- The printed dot area depends predominantly on the wetting interaction.

GRAPHICAL ABSTRACT

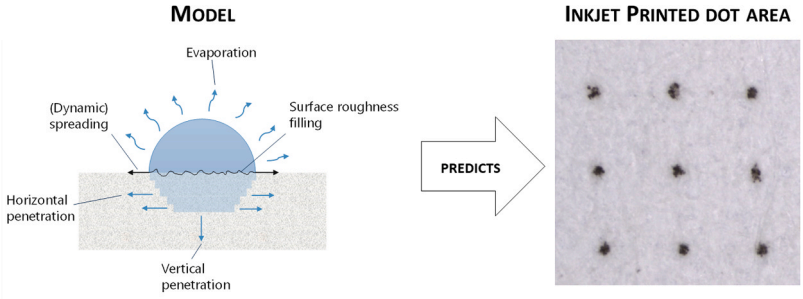

ARTICLE INFO

Keywords:
Inkjet
Liquid penetration
Wetting
Picoliter drop
Porous sheet
Print quality

ABSTRACT

Spreading and absorption of small liquid drops on porous substrates is of interest in a number of fields ranging from additive manufacturing and composite processing to inkjet printing. In inkjet printing, spreading and absorption processes determine the final area of a printed dot, which is decisive for print quality in terms of coverage and resolution. However, it is not fully understood how substrate and liquid properties influence the involved physical processes and the resultant printed dot area. In this work, the printed dot area of overall 140 paper-liquid pairings representative for the operational window of an inkjet printer is evaluated. The results are explained by a simple model including spreading, absorption, and evaporation. The surface tension and viscosity of the liquids, as well as the pore size and polarity of the substrates were varied systematically to represent the range of uncoated paper-liquid pairings applicable for inkjet printing. Results show that the printed dot area mainly depends on the wettability of the liquid-substrate pairing followed by penetration speed. Evaporation and volume reduction due to roughness filling had little impact. The modeling results are in line with empirical observations showing that the dot area is closely related to the contact angle.

1. Introduction

Spreading and absorption of small liquid drops into porous substrates is of interest in a number of fields ranging from additive manufacturing [1] and composite processing [2] to printed electronics [3], textiles [4] and inkjet printing [5]. It is a complex phenomenon starting with the

* Corresponding author at: Institute of Bioproducts and Paper Technology, Graz University of Technology, Inffeldgasse 23, 8010 Graz, Austria.
E-mail address: ulrich.hirn@tugraz.at (U. Hirn).

https://doi.org/10.1016/j.colsurfa.2023.131986
Received 20 April 2023; Received in revised form 23 June 2023; Accepted 30 June 2023
Available online 1 July 2023

drop impact on the porous solid, followed by spreading, absorption and evaporation of the liquid. Several studies addressed the topic experimentally (e.g. [2,6–16]), although the involved size and time scales relevant for applications like inkjet printing – picoliters and milliseconds – remain challenging. Since reliable experimental data are difficult to obtain, many attempts have been made to simulate the spreading and absorption of liquid drops on porous substrates. The approaches range from rather simple models mostly relying on adaptations of the Lucas-Washburn/Darcy equation to describe liquid absorption (e.g. [9, 11,12,17–20]), to a wide variety of numerical simulations [1,8,10,13, 14,17,21–29] mostly applying the volume of fluid (VOF) [1,10,23,26, 28], or Lattice Boltzmann [3,21,22] methods.

In general, spreading and absorption are often seen as competing processes during which fast absorption limits the extent of spreading [11,13,22,23,30], although Tan [10] argues that spreading and absorption happen at different time scales and can be seen as decoupled processes. The process of drop spreading and absorption is further complicated by simultaneous evaporation which can limit penetration [20,28,31]. Nonetheless, evaporation is neglected in most studies. Surface roughness can additionally limit the extent of spreading [26] and the drop can be distorted by the surface topography [21].

Numerical studies are often validated only by theoretical considerations. If experimental results are used for validation, the measurements were usually done only for a few liquids and/or substrates. Given the complexity of the problem, it is not surprising that most numerical studies focus on spreading and absorption while neglecting evaporation and roughness. Without comprehensive experimental validation it however is not clear if all relevant processes are captured. To improve the understanding of drop absorption on porous media and of model validity, it would be necessary to experimentally study a broad range of substrates and liquids which differ in the properties most relevant for drop absorption and spreading such as viscosity, surface tension, hydrophilicity, porosity, roughness etc. Therefore, the aim of this work is twofold:

- To study a large set of liquids and uncoated paper substrates and to describe the experimental observations with a simple model for dot spreading.
- To quantify the relevance of wetting, penetration, evaporation and (to some extent) substrate roughness on the resulting printed dots.

As this work focuses on uncoated paper substrates, it needs to be pointed out that the results might not be transferable to coated paper substrates as those have shorter and more fine capillaries which can cause differences in the absorption behavior (e.g. impact of inertia on absorption, compare [32]).

2. Materials and methods

To capture the impact of the most relevant substrate and liquid properties on inkjet printed picoliter dots, five liquids with varying surface tension and viscosity were printed on two sets of paper substrates. For both sets, the substrate pore size and polarity were varied systematically. Single dot patterns were printed with 18 pL drops and analyzed via image analysis. Finally, the measured printed dot area was predicted by a simple model combining drop spreading, absorption, and evaporation as well as surface roughness filling.

2.1. Liquids

The five liquids used for printing are mixtures of deionized water, glycerol (AnalaR®NORMAPUR® from VWR, 99.5%), 1,2-hexanediol (Alfa Aesar from Thermo Fisher Scientific, 97%), and a dye (Naphthol Blue Black, 100%) (compositions can be found in Table 1, TL referring to "test liquid"). Glycerol was used to modify the viscosity, while 1,2-hexanediol lowers the surface tension. The liquid compositions were adjusted to approximately represent the range of liquids that can be printed in an inkjet printer in terms of viscosity and surface tension [5]. The viscosity and surface tension of the liquids are shown in Fig. 1.

Two dimensionless parameters – the Ohnesorge number *Oh* (Eq. (1)) and the Reynolds number *Re* (Eq. (2)) – can be used to assess the jettability of a liquid [33]. Thereby the viscosity η, the surface tension γ and the density ρ varied for the test liquids, while the jetting speed v (8 m s^{-1}) and the nozzle width l (20 µm) were constant for all trials. Fig. 2 compares the theoretical window of printable fluids as indicated by *Re* and *Oh* with the liquids used in this work. Obviously, the actual jetting window of the employed printhead differs somewhat from what is predicted theoretically.

$$Oh = \frac{\eta}{\sqrt{\gamma \rho l}} \tag{1}$$

$$\mathrm{Re} = \frac{\rho v l}{\eta} \tag{2}$$

For the surface tension measurement, a Dataphysics OCA200 and the pendant drop method was used. Liquid density was measured with a Mettler-Toledo DE40 instrument (oscillating u-tube). An Anton Paar

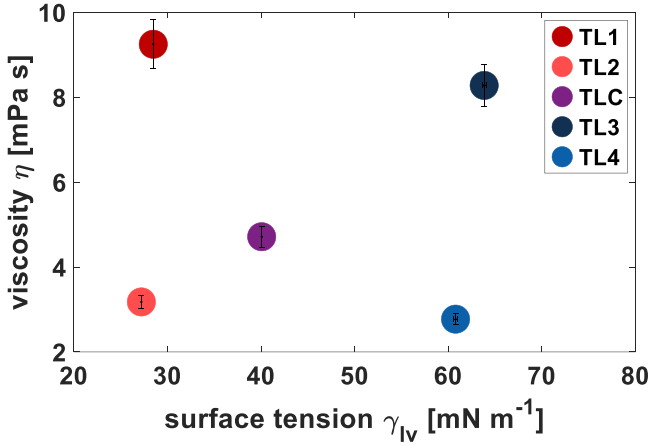

Fig. 1. Properties of the printing liquids used. High surface tension liquids are represented by blue markers, low surface tension by red ones. A higher viscosity is indicated by a darker color. Error bars indicate 95% confidence intervals.

Table 1
Composition and properties of test liquids. Composition is given in gram. Surface tension components were calculated from interfacial tension measurements in n-hexane using the OWRK theory. Measurements were performed at 23 °C and 50% relative humidity.

Test liquid	Water [g]	Glycerol [g]	Hexane-diol [g]	Dye [g]	Density ρ [kg m^{-3}]	Viscosity η [mPa s]	Surface tension γ_{lv} [mN m^{-1}]	Disper-sive surface tension γ_l^d [mN m^{-1}]	Polar surface tension γ_l^p [mN m^{-1}]	Evapo-ration rate [µL mm^{-2} s^{-1}]
TL1	41.9	48.0	10.0	0.3	1117.2	9.248	28.5	27.4	1.1	0.108
TL2	64.9	25.0	10.0	0.3	1058.7	3.178	27.2	26.2	1.0	0.094
TL3	42.4	57.5	-	0.3	1146.2	8.278	63.8	35.5	28.3	0.031
TL4	64.8	35.0	0.1	0.3	1085.0	2.772	60.8	33.2	27.6	0.024
TLC	56.4	42.0	1.5	0.3	1111.7	4.714	40.1	25.5	14.6	0.100

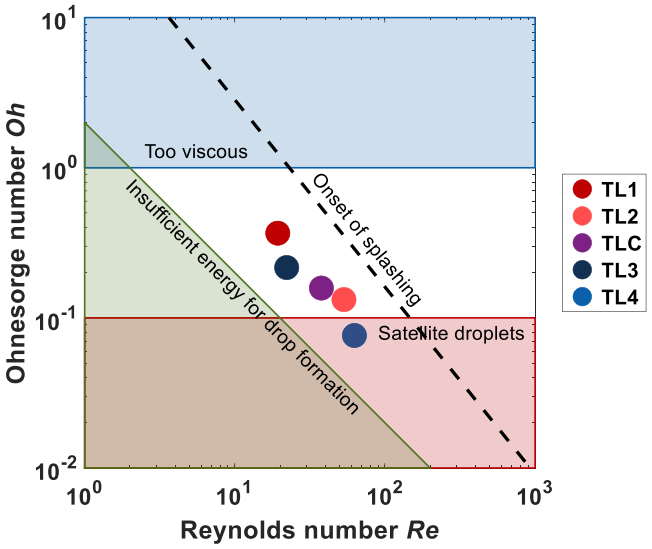

Fig. 2. Printable fluid window indicated by Reynolds and Ohnesorge number [33] compared to liquids used in this work.

MCR 100 device with a double-gap concentric cylinder system (DG 26.7) was used for the viscosity measurements. The shear rate was kept constant at 1000 s^{-1} and the liquids were pre-sheared for 5 min at 20 °C. During the measurement, the temperature was increased stepwise by 5 °C. The reported viscosity values were interpolated to 23 °C, since all other measurements were performed at climatized conditions of 23 °C and 50% relative humidity (ISO 187). Furthermore, polar and dispersive contributions of the surface tension γ_l^p, γ_l^d were calculated from interfacial tension measurements of the test liquids in n-hexane (from Merck KGaA, 99%) using the Owens-Wendt-Rabel-Kaelble (OWRK) theory [34–36]. The interfacial tension was determined from liquid-liquid pendant drop measurements, again using a Dataphysics OCA200. Pendant drops of the test liquids were formed in a cuvette that was filled with n-hexane. More details regarding this measurement can be found in [37].

2.2. Substrates

To represent the range of uncoated paper substrates that are used in inkjet printing, two sets of trial substrates were used. For both sets, the substrate pore size and the polarity were varied systematically.

2.2.1. Production of the substrates

The first set is based on a rather porous, industrially produced printing base paper with a grammage of 89.6 g m^{-2} and is further on referred to as "industrial papers". It is made up of bleached pulp (mainly eucalyptus) and 21% scalenohedral precipitated calcium carbonate fillers. The pore size and polarity of the paper were modified after production. Chemical vapor deposition was used to obtain four polarity levels by applying either 0, 10, 20, or 40 mL of hexamethyldisilazane (HMDS, from Carl Roth, 98%) per 10 A4 sheets. The hydrophobization reaction took place at 60 °C and 500 mbar for a duration of 24 h. The treatment led to a lower polarity of the papers indicated by a higher water contact angle as shown in Fig. 3(a) (as measured for surface energy determination; H followed by a number stands for the amount of HMDS applied). After the chemical vapor deposition, the substrate pore size was reduced by calendering using a lab calendar at room temperature. Four pore size levels were obtained by applying forces of 0, 15, 30, or 60 kN respectively. Fig. 3(a) shows that the calendering led to a reduction of air permeance (measured with the Gurley method, ISO 5636–5; C followed by a number stands for the calendering force). Combining the four polarity and four pore size levels resulted in 16 different paper types for the industrial paper series.

The advantage of the first approach is that the substrate polarity and pore size can be varied independently. A second set of trial substrates (further on referred to as "lab papers") was used in addition to vary substrate pore size and polarity in a way closer to industrial paper making. Laboratory hand sheets with a grammage of 80 g m^{-2} were produced from ECF bleached eucalyptus kraft pulp without fillers on a Rapid-Köthen sheet former (DIN EN ISO 5269–2). The pore size of the substrates was modified via refining of the pulp in a valley beater (ISO 5264–1) for either 0, 11, 28, or 47 min. The polarity of the substrates was changed via alkyl ketene dimer (AKD) sizing by adding either 0, 2.5, or 5 kg per tonne of dry mass pulp of a 20% AKD emulsion to the pulp suspension. Fig. 3(b) shows the water contact angle and Gurley air permeance of the resulting 12 lab papers (R followed by a number stands for the refining intensity, S followed by a number stands for the AKD sizing intensity, higher numbers meaning more intensive treatment). As expected, the AKD sizing led to higher water contact angles while the refining reduced the air permeance. Overall, a bigger pore size range could be achieved via refining. More details on the production of the trial papers can be found in [38,39].

2.2.2. Substrate properties

To characterize the substrate polarity, surface energy components were determined according to OWRK theory. Contact angles of deionized water, ethylene glycol (from Carl Roth, 99%) and diiodomethane (ReagentPlus® from Sigma Aldrich, 99%) were measured on all papers

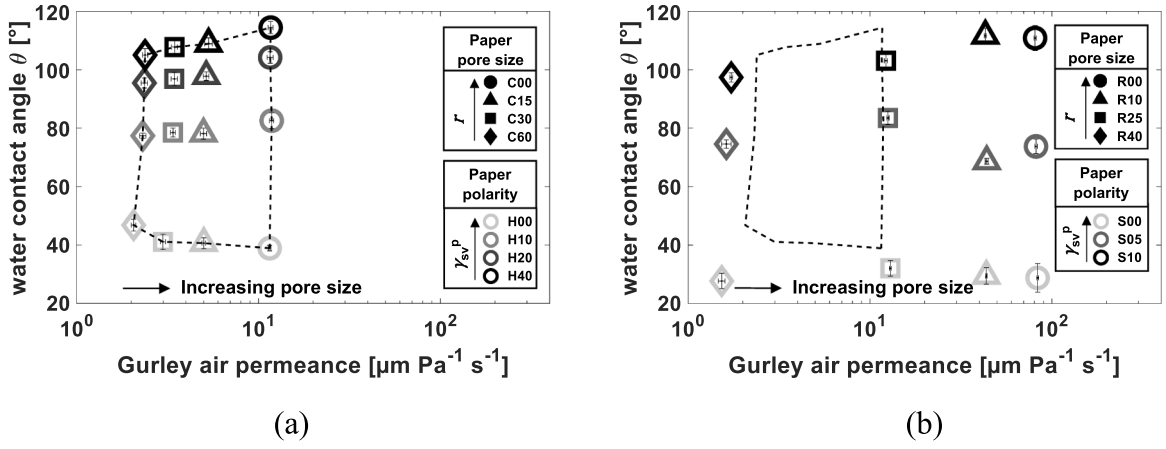

Fig. 3. Water contact angle and air permeance of the trial papers: (a) industrial papers; (b) lab papers. Substrate pore size is represented by the marker symbol, substrate polarity by the marker edge gray value, a brighter gray meaning a higher polarity.

with a Dataphysics OCA200 using 2 μL drops. Further details on the surface energy measurements can be found in [37]. The resulting polar and dispersive surface energy components γ_s^p, γ_s^d are reported in Table 2. For both trial series, the hydrophobization treatment using either HMDS or AKD dramatically reduced the polar part of the surface energy while having a smaller effect on the dispersive part.

Substrate pore size was determined via mercury porosimetry using an Autopore IV 9500 instrument from Micromeritics Instrument Corp. Since papers of the same calendering/refining treatment showed no significant differences in air permeance, mercury porosimetry measurements were performed only for papers with the highest polarity (labelled H00 or S00). A mean weighted pore diameter was calculated from the mercury intrusion curves and used in the simulation of the industrial papers.

However, no plausible results could be obtained for the lab paper data set due to the high porosity of the unrefined papers. To estimate the pore size of the lab papers, the law of Hagen-Poiseuille (Eq. (3)) was therefore used instead. The Gurley air permeance P thereby is a volumetric air flow $\dot{V}$, averaged over the measurement area and pressure. Accordingly, the pore radius r is proportional to the air permeance P, the viscosity of air η, and the thickness of the substrate x (Eq. (4)). Since the air permeance is averaged over the measurement area, the result of Eq. (4) however would have the dimension of $\mu m^{0.5}$ instead of μm. Therefore, Eq. (4) needs to be corrected by a pore area estimate A_{fit} which is obtained from a fit of the calculated pore diameters vs. the mercury porosimetry pore diameters of the industrial papers (R^2=0.95, results and more details can be found in the electronic supplementary info, ESI). The data of the industrial papers could be used to obtain A_{fit} since the mercury porosimetry measurement was successful for those papers. The pore diameters used for the simulations are reported in Table 2. Thickness and apparent density were measured according to DIN EN ISO 534.

$$\dot{V} = \frac{\pi \bullet r^4}{8 \bullet \eta} \frac{\partial p}{\partial x} \tag{3}$$

$$r = \left(\frac{P \bullet 8 \bullet \eta \bullet x \bullet A_{fit}}{\pi} \right)^{0.25} \tag{4}$$

2.3. Printing trials and printed dot evaluation

A single dot pattern was printed with the five test liquids on each of the 28 paper types described above. The dot pattern was applied with a commercial inkjet printhead as it is used in the Canon Colorstream 3000 industrial high speed inkjet printer. The piezo-electric printhead creates drops on demand and is operated at a frequency of up to 40 kHz. The resolution is 600 dpi. The drop size was set to 18 pL by adjusting waveforms and printhead voltage for each liquid. The drop volume thereby was evaluated by weighing a fully printed sheet immediately after printing and dividing the result by the number of printed drops. The printing speed used was 7.5 m min^{-1}, implying that an A4 sheet is printed in about 2.4 s. Due to the fast absorption of the paper substrates and the low liquid volume applied, no external drying/fixation treatment had to be used.

After printing, images of the prints were recorded using an ImageXpert Motion System equipped with a color camera with an image size of 4800 × 3600 and a camera resolution of 3.7 μm per pixel. To ensure that the resulting images were not affected by opacity differences of the papers, the printed samples were placed on top of a staple of unprinted samples of the same paper type for imaging. To accommodate for uneven lighting, a reference image of a white ceramic tile was taken. Shading correction of the recorded images was performed by subtracting the image of the ceramic tile from the images of the printed dots. Per test point, two A5 sheets were printed and three images at different positions were taken on each sheet. One image included about 400 printed dots which results in about 2400 evaluated inkjet dots per test point.

The contrast of the printed dots on the background was poor (compare Fig. 4(a)) and therefore automatic evaluation with the ImageXpert software was not possible. Instead, a digital analysis software was developed in MATLAB for dot evaluation. Thereby, the original image was first transformed by subtracting the blue color channel

Table 2
Properties of the paper substrates. Reported errors are 95% confidence intervals. Measurements were performed at 23 °C and 50% relative humidity. *Lab paper pore size was estimated from Gurley air permeance.

Paper	Thickness [μm]	Apparent density [g cm^{-3}]	Gurley air permeance [μm Pa^{-1} s^{-1}]	Mean pore diameter [μm]	Disper-sive surface energy γ_s^d [mN m^{-1}]	Polar surface energy γ_s^p [mN m^{-1}]	Roughness – void volume of the surface [mL m^{-2}]
C00_H00	132.4 ± 1.9	0.68	11.5 ± 0.2	2.80	20.3	25.3	1.08
C00_H10	134.3 ± 2.5	0.67	11.9 ± 0.3	2.80	37.8	1.1	1.09
C00_H20	132.4 ± 1.7	0.68	11.6 ± 0.5	2.80	33.6	0.0	1.07
C00_H40	132.0 ± 2.8	0.68	11.7 ± 0.4	2.80	23.6	0.0	1.13
C15_H00	100.0 ± 1.2	0.90	5.0 ± 0.1	2.16	21.8	23.5	0.69
C15_H10	99.1 ± 2.0	0.91	5.0 ± 0.2	2.16	36.1	2.5	0.69
C15_H20	100.8 ± 1.9	0.89	5.2 ± 0.2	2.16	38.3	0.0	0.69
C15_H40	99.9 ± 1.9	0.90	5.3 ± 0.3	2.16	32.0	0.0	0.70
C30_H00	94.9 ± 2.6	0.94	3.0 ± 0.1	1.89	22.2	23.7	0.65
C30_H10	95.8 ± 3.1	0.93	3.4 ± 0.1	1.89	36.4	2.40	0.64
C30_H20	94.8 ± 1.8	0.94	3.5 ± 0.1	1.89	39.8	0.0	0.64
C30_H40	94.6 ± 1.7	0.94	3.5 ± 0.1	1.89	32.2	0.0	0.65
C60_H00	92.3 ± 2.1	0.97	2.1 ± 0.1	1.51	25.1	19.5	0.69
C60_H10	91.8 ± 1.7	0.97	2.3 ± 0.1	1.51	34.1	3.20	0.64
C60_H20	91.1 ± 2.7	0.98	2.4 ± 0.1	1.51	41.0	0.0	0.64
C60_H40	92.2 ± 1.5	0.97	2.4 ± 0.1	1.51	34.1	0.0	0.65
R00_S00	151.9 ± 0.9	0.53	83.6 ± 1.1	4.68*	19.9	30.6	1.10
R00_S05	153.0 ± 1.0	0.52	81.9 ± 1.4	4.66*	33.9	4.0	1.10
R00_S10	152.6 ± 1.3	0.52	80.9 ± 1.3	4.65*	34.1	0.0	1.09
R10_S00	140.5 ± 0.6	0.57	43.7 ± 0.4	3.90*	20.4	29.2	1.04
R10_S05	139.5 ± 1.5	0.58	43.9 ± 0.9	3.90*	30.8	5.8	1.04
R10_S10	138.4 ± 0.6	0.58	43.1 ± 0.6	3.87*	33.1	0.0	1.02
R25_S00	125.3 ± 0.8	0.64	13.0 ± 0.2	2.80*	19.0	29.0	0.96
R25_S05	125.9 ± 0.7	0.64	12.6 ± 0.2	2.78*	35.4	1.3	0.95
R25_S10	125.3 ± 0.7	0.64	12.3 ± 0.3	2.76*	35.9	0.0	0.93
R40_S00	111.3 ± 0.9	0.72	1.5 ± 0.1	1.59*	18.2	31.4	0.84
R40_S05	111.9 ± 2.0	0.71	1.6 ± 0.1	1.62*	30.1	4.5	0.83
R40_S10	112.0 ± 1.0	0.71	1.7 ± 0.0	1.64*	38.1	0.0	0.83

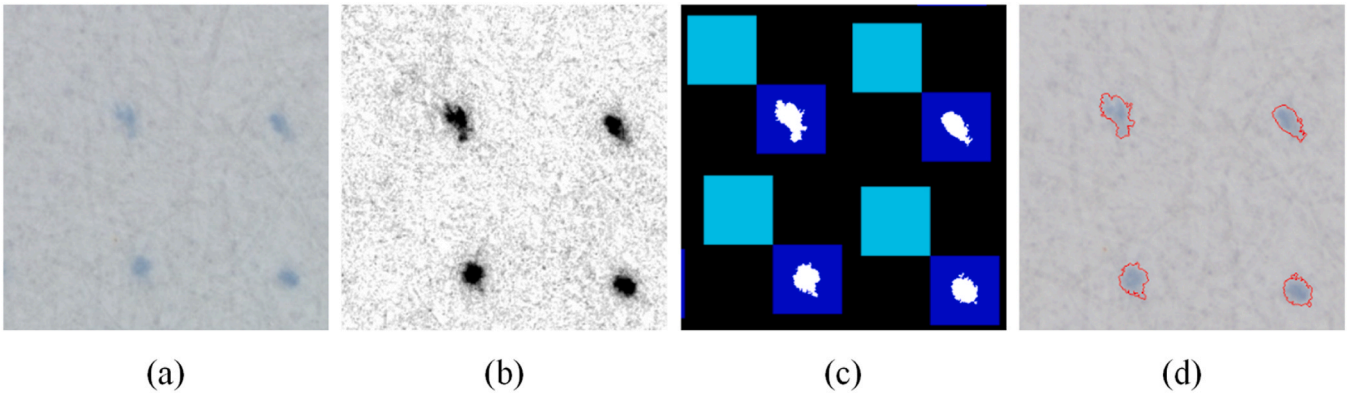

Fig. 4. Image analysis for printed dot detection – processing steps: (a) originally recorded image; (b) image transformed via color channel subtraction used for binarization; (c) detected dot (white), square around the dot (blue) and square for background evaluation (cyan); comparison of light absorption from detected dots and squares around the dots is used to evaluate the quality of the dot detection; (d) finally detected dot on original image (corrected for uneven lighting).

from the red color channel and amplifying the result (Fig. 4(b)). The blue dots were visible mainly in the red channel and hardly in the blue channel. Thanks to the subtraction, the background structure of the sheet could be eliminated to a large extent, leading to a better visibility of the printed dots. This grayscale image could then be used for binarization (compare electronic supplementary information, ESI). Fig. 4(c) shows the detected dots after binarization. Additionally, one set of squares was defined surrounding the dots (colored in blue), another set of squares was defined for evaluation of the background (in cyan). Area, perimeter, color intensity (evaluated from the red channel of the original image), aspect ratio (axis ratio of fitted ellipse), and orientation of the detected dots were evaluated. The light absorption LA_{dot} [8 bit gray value μm^2] can be calculated from the detected parameters according to Eq. (5).

$$LA_{dot} = \Delta GV_{dot} \bullet A_{dot} \tag{5}$$

The area of the dot A_{dot} [μm^2] is multiplied with the difference in gray value ΔGV_{dot} [8 bit gray value] between the dot and the background. Furthermore, the light absorption can also be calculated using the blue squares (LA_{square} [8 bit gray value]). The difference between the mean gray value of the square including the dot and the background gray value is a measure of light absorption, as it is influenced by both size and intensity of the dot within the square (Eq. (6)).

$$LA_{square} = \Delta GV_{square} \tag{6}$$

The area surrounding the dot should not affect the LA_{square} as it will have the same intensity as the background on average. If the LA_{dot} is further averaged by the square size used for the calculation of LA_{square}, both values are directly comparable and in the case of a perfectly sharp detection would result in the same value. The comparison between LA_{dot} and LA_{square} can therefore be used to evaluate the quality of the detection. After optimizing the binarization, a high R^2 of LA_{dot} vs. LA_{square} could be reached for both trial series (R^2=0.92 for industrial papers, R^2=0.95 for lab papers). This proves that the dot sizes are detected consistently even for cases where the color intensity is particularly low. At the same time, the threshold with the smallest dot size that still delivered a high R^2 ($R^2 > 0.9$) was chosen in order to make sure that the dot size was not overestimated. The finally detected dots on the original image are shown in Fig. 4(d). For more information on threshold selection for the binarization and evaluation of the dot detection using LA_{dot} and LA_{square} please refer to the ESI.

2.4. Modeling concept

The area covered by printed dots is the result of several dynamic processes taking place simultaneously. After the impact of the drop on the substrate, the drop spreads on the surface, while liquid is absorbed into the porous substrate and liquid evaporates. The modeling concept used in this work is shown schematically in Fig. 5. The spreading behavior can influence the final dot area via the wettability and the spreading speed. A high wettability will generally lead to a big dot. The spreading speed is important in case the extent of spreading is not only limited by the wettability but also by fast absorption limiting the volume available for spreading. As mentioned earlier, absorption and spreading are seen as competing processes in many studies (e.g. [11,13,22,23]). More generally this means that anything that reduces the liquid volume available for spreading can potentially influence the final dot area. Therefore, also evaporation of the liquid and surface roughness filling will be considered in the model. Furthermore, lateral penetration not only increases the absorbed volume but also the finally covered area at the surface. The details for each model component will be discussed in the following sections. Finally, some parameters had to be corrected for the size- and time scale, which will be discussed in Section 2.4.5.

In general, it needs to be noted that the present model is not a first principles physical model. The aim was to describe the processes of penetration, spreading, evaporation and roughness filling in a rather simple, data driven way as it is interesting how each of these processes contribute to the final printed dot area from an engineering point of view.

A flowchart of the model can be found in Fig. 6. The model starts with a spherical drop with an initial volume of 18 pL at $t_0 = 0$ s. Then, the penetration depth for the first time step $h(t_1)$ [μm] is calculated as

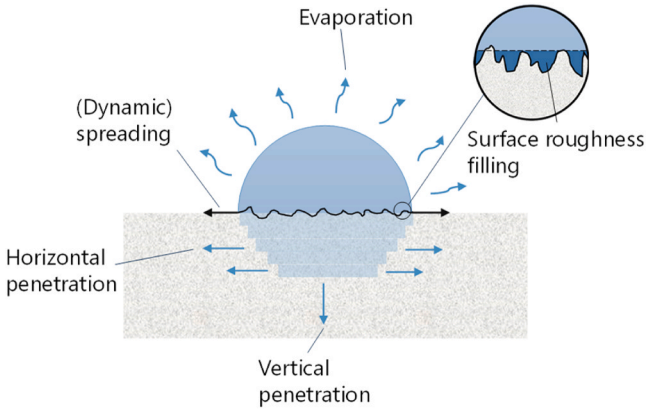

Fig. 5. Modeling concept. Printed dot area is simulated as a result of simultaneous spreading, absorption and evaporation. Lateral penetration and surface roughness reduce the drop volume. Lateral penetration also increases the printed dot area.

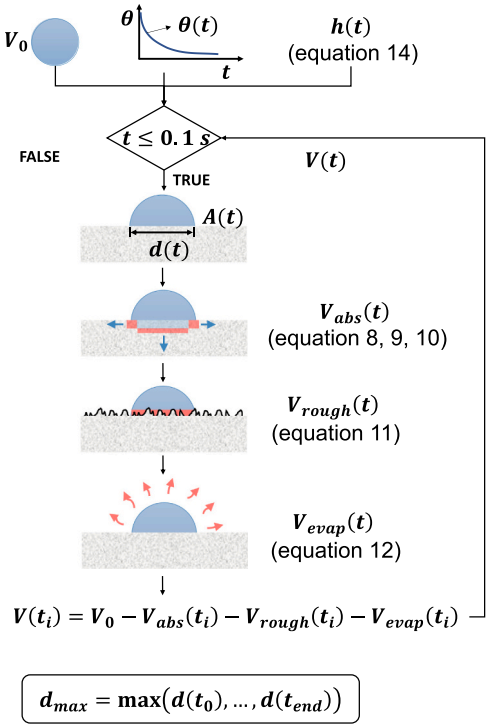

Fig. 6. Model flowchart. Remaining drop volume $V(t)$ and corresponding drop base diameter $d(t)$ are calculated for each time step. The maximum occurring base diameter (plus lateral penetration) d_{max} is used for the prediction of the inkjet printed dot area.

described in Section 2.4.1. In order to be able to calculate the absorbed volume at this time step $V_{abs}(t_1)$ [μm^3], the area covered by the drop at t_1 has to be calculated. This can be done if it is assumed that the drop shape resembles the cap of a sphere. Knowing the contact angle θ at t_1 (from the data described in Section 2.4.2) and the initial volume $V(t_0)$, the base diameter $d(t_1)$ [μm] and consequently the covered area $A(t_1)$ [μm^2] can be calculated. Multiplying the penetration depth $h(t_1)$ with the area covered, the absorbed volume can be calculated (Eq. (7)).

$$V_{abs}(t_1) = h(t_1)\cdot A(\theta(t_1), V(t_0)) \tag{7}$$

In order to account for lateral penetration, we assume the same penetration speed in vertical and lateral direction. This is a rough assumption that was made for the sake of simplicity. In fact, the penetration speed in paper differs in vertical and lateral directions, as well as between machine direction and cross direction, due to the oriented geometrical structure [40], which was not considered in this analysis. The area A is increased by adding the penetration depth $h(t)$ to the diameter depending on the contact time. If we are for example calculating the absorbed volume for the second time step, the area covered at the second time step will be calculated using the volume remaining after t_1. The volume already absorbed in the first time step will be increased by the amount of lateral penetration (second half of Eq. (8)). The total absorbed volume after the second time step is therefore calculated as two segments according to Eq. (8). The same principle is applied to all further time steps.

$$V_{abs}(t_2) = h(t_1)\cdot A(\theta(t_2), V(t_1)) + h(t_2)\cdot(d(t_1) + 2\cdot h(t_2 - t_1))^2\cdot\frac{\pi}{4} \tag{8}$$

Eq. (8) can be written in a more general form. The time t_i is thereby calculated from the number of time steps Δt (Eq. (9)). Δt was set to 20 μs. The total absorbed volume at each time t_i can then be calculated with Eq. (10).

$$t_i = t_0 + i\cdot\Delta t \text{with} t_0 = 0 \text{and} \Delta t = 0.00002s \tag{9}$$

$$V_{abs}(t_i) = h(t_1)\cdot A(t_i) + \sum_{n=2}^{i} h(t_n)\cdot(d(t_{i-n+1}) + 2\cdot h(t_0 + (n-1)\cdot\Delta t))^2\cdot\frac{\pi}{4} \tag{10}$$

The covered area is further used to calculate the volume captured within the surface roughness profile. For that, the specific void volume of the surface V_{void} [μm^3 μm^{-2}] is multiplied with the area A [μm^2]. The volume captured within the roughness profile will not decrease once the drop becomes smaller than its maximum extent due to ongoing penetration and evaporation. Therefore, always the maximum drop area that has been reached until the respective point in time t_i is used for the calculation of the volume captured due to roughness V_{rough} (Eq. (11)).

$$V_{rough}(t_i) = V_{void}\cdot\max(A(t_0), \ldots, A(t_i)) \tag{11}$$

Similarly as for the area calculation, the contact angle $\theta(t_i)$ at time t_i and the volume of the earlier time step $V(t_{i-1})$ are used to calculate the surface area $S(t_i)$ [μm^2] of the drop which is in contact with the surrounding air. The surface area is needed to then calculate the amount of liquid that is evaporated at each time step by multiplying it with the evaporation rate E [μm^3 μm^{-2} s^{-1}] and the time step interval Δt [s]. The evaporated amounts during each time step are summed up to give the total evaporated amount after time t_i (Eq. (12)).

$$V_{evap}(t_i) = \sum_{n=1}^{i} S(t_n)\cdot E\cdot\Delta t \tag{12}$$

Finally, the remaining volume after each time step can be calculated with Eq. (13). The remaining volume is then used to compute the covered substrate area and surface area of the drop needed to calculate the absorbed and evaporated volume in the next time step. This process was repeated until a simulation time of 0.1 s. After this time, the remaining drop volume was zero for all of the simulated drops which were absorbed into the paper. The maximum base diameter also considering lateral penetration was used for comparison to the measured printed dots.

$$V(t_i) = V(t_0) - V_{abs}(t_i) - V_{rough}(t_i) - V_{evap}(t_i) \tag{13}$$

2.4.1. Liquid penetration

In order to be able to separate the effects of drop spreading and absorption in theory, the absorbed drop volume needs to be calculated from the penetration depth together with the area covered by the drop. From a theoretical point of view, the penetration depth then is independent of the spreading speed, while the absorbed amount depends on the drop contact area and thus on the extent of spreading at each point in time. As the penetration depth is difficult to measure, the Lucas-Washburn equation [41,42] was used to describe the penetration. The contact angle in the Lucas-Washburn (LW) equation, however, was replaced by liquid and substrate surface energies using the OWRK theory resulting in Eq. (14) for the time dependent penetration depth h. Thereby, r is the pore radius [m], γ_{lv} the liquid surface tension, γ_l^p the polar and γ_l^d the dispersive part of the surface tension, γ_s^p the polar and γ_s^d the dispersive parts of the substrate surface energy [N m^{-1}], η the dynamic viscosity [Pa s] and t the time [s]. This model equation has been introduced and validated earlier (compare [37]). The benefit of the combined LW-OWRK equation is that unlike the classical LW equation it only contains substrate and liquid properties that are independent of each other. The measured substrate and liquid properties used in Eq. (14) are reported in Table 1 and Table 2 respectively.

$$h = \sqrt{\frac{r \bullet (2\sqrt{\gamma_s^d \bullet \gamma_l^d} + 2\sqrt{\gamma_s^p \bullet \gamma_l^p} - \gamma_{lv})}{2\eta} \bullet t} \tag{14}$$

2.4.2. Spreading

To describe the spreading behavior and to calculate the volume absorbed due to penetration in the model, information about the contact angle of each liquid-substrate pairing over time is needed. Models

describing the wetting dynamics like the hydrodynamic or the molecular kinetic models were not able to describe the wetting dynamics on paper probably due to the influence of surface roughness and surface chemistry [16,43]. Furthermore, these models contain parameters which are hard or impossible to measure like the molecular slip length in the hydrodynamic model or the molecular jump length and -frequency in the molecular kinetic model. Therefore, dynamic contact angle measurements with the test liquids were performed on all papers using a Fibro DAT 1100 dynamic contact angle instrument. The Fibro DAT was chosen because it deposits the drops on the surface with a fast downward and back upward motion of the capillary, thanks to which it is possible to avoid penetration during drop deposition. The drop size was 3.5 μL. Microliter drops were chosen because it is difficult to obtain representative results using smaller (i.e. picoliter) drops. For picoliter drops there not only is a large degree of scattering due to surface inhomogeneities, some drops are not even recorded at 2000 frames per second if they fall into a valley of the paper surface. Furthermore, contact angles of microliter drops correlated similarly well or even better with printed dot area than contact angles from picoliter drops in earlier work [44].

In order to be able to calculate the contact angle θ at any point in time, a power law ($\theta = a \bullet t^b$) was fitted to the measured contact angle curves. To minimize the influence of absorption on the contact angle curves, the fit was performed only until the point at which the maximum extent of spreading (maximum drop base diameter) had been reached. An example for a measured and a fitted curve is shown in Fig. 7. The fitted functions were used for the model calculations, after adapting the size- and timescale to picoliter drops, as described in Section 2.4.5.

2.4.3. Evaporation

In order to estimate evaporation rates for the printing liquids, picoliter drops were deposited on aluminum foil and the volume was recorded over time. Picoliter drops were used to determine the evaporation behavior because the problems encountered on rough and porous substrates are not an issue in the case of aluminum foil. Moreover, the evaporation rates decreased quickly after drop deposition probably due to saturation of the surrounding air and it therefore seemed important to measure the drops in the relevant size scale.

For this purpose, a Dataphysics OCA200 equipped with a picoliter dosing system was used. The aluminum foil was bent around a tube which was fixed on a plate. This was necessary because of the small drop size: depositing the drops on the highest elevation of the tube optimizes the drop visibility in the recording. For all liquids, 30, 60 and 120 pL drops were measured at a frame rate of 2000 s^{-1}. 20 drops were measured per liquid and drop size. Outliers in terms of initial contact angle and/or volume were removed.

As mentioned before, the volume reduction slowed down with time probably due to saturation effects. As the paper samples were in motion during and shortly after the printing process, less saturation is expected in the printing trial. Therefore, we decided to determine the evaporation rate for the first 10 ms after drop deposition in order to reduce saturation effects. Also, many drops will be depleted within a few milliseconds in the printing setting and 10 ms thus is in the relevant time scale. The volume loss was averaged over the surface area of the drop before calculating the mean evaporation rate. The measured evaporation rates are shown in Fig. 8. Water was measured as a reference. Although the error bars are rather large, the different drop sizes show the same trend. Liquids with a high surface tension (TL3, TL4) have lower evaporation rates similar to water while the evaporation rates of lower surface tension liquids are significantly higher. The mean evaporation rate of all three drop sizes was used for the model calculations. A constant evaporation rate was assumed and the evaporated volume was calculated by multiplying the evaporation rate with the surface area of the drop for each time step (Eq. (12)).

2.4.4. Roughness

The surface roughness can influence the final dot area in several ways. Its potential impact on spreading in terms of wettability and spreading speed is already captured in the contact angle measurements described in Section 2.4.2. Besides spreading, roughness can also influence the printed dot area as liquid volume is held in the valleys between the rough peaks (compare the darker colored liquid in the enlarged representation of the roughness in Fig. 5). Due to the small size of the printed drops, the drop volume might be significantly reduced by the surface roughness. To estimate the volume reduction due to surface roughness, the surface structure of the paper substrates was captured with the shape-from-focus method with an infinite focus microscope (IFM) from Alicona. The void volume of the surface was evaluated after applying a fast Fourier transformation (FFT) high pass filter. A threshold wavelength of 100 μm was used, as this is the size scale of the printed dots. For the sensitivity analysis (Section 4), also filter wavelengths of 150, 200, 300 and 500 μm were applied. The void volume of the surface is defined as the sum of the void volume of the valleys and the core and comprises the volume enclosed within 90% of all heights. The results for a filter wavelength of 100 μm are reported in Table 2. To calculate the drop volume captured by roughness filling in the model, the maximum area covered by the drop until each point in time was multiplied with the (area specific) void volume of the surface (Eq. (11)).

2.4.5. Correction of size and time scale

Surface roughness and evaporation rates were determined in the relevant time and size scales. Spreading and penetration however need to be adjusted by a factor to adapt the measurements to the relevant

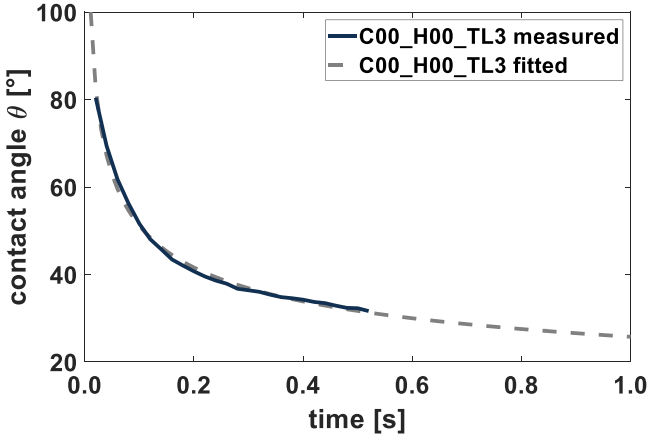

Fig. 7. Example for measured contact angle over time (blue line) and the corresponding power law fit (dashed grey line).

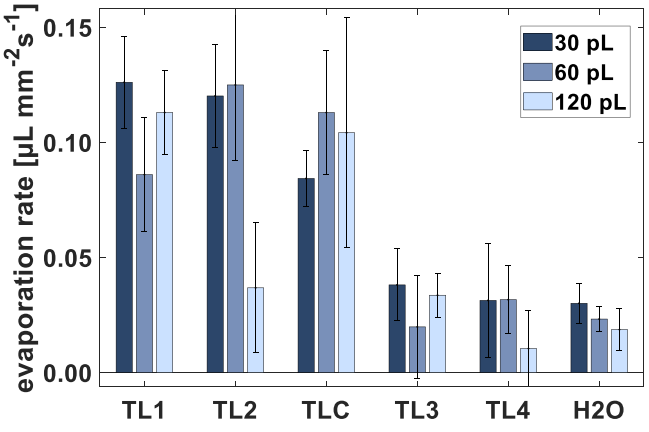

Fig. 8. Evaporation rates of the test liquid determined from 30, 60, and 120 pL drops for the first 10 ms after drop deposition. Error bars indicate 95% confidence intervals.

scales. These adjustments were made by comparing simulated results with measurements of 30 pL drops on the untreated industrial base paper using the same setup as for the evaporation rate measurements.

2.4.5.1. Spreading. As explained in Section 2.4.2, the contact angle measurements were performed with 3.5 μL drops because bigger drops are less affected by local inhomogeneities. Furthermore, the measurements of picoliter drops on paper cannot be fully representative because some drops fall into the valleys of the surface and cannot be tracked. Nonetheless, the microliter drops spread slower than the picoliter drops. The measured results thus need to be rescaled to accommodate for the faster spreading of the picoliter drops used for printing. This is done by multiplying the time in the power law with a factor x ($\theta = a \bullet (t \bullet x)^b$). To determine how much the measured contact angle curves need to be sped up, the scaled power law curves are compared to measurements of 30 pL drops on the untreated industrial paper with all test liquids. The sum of squared error is minimized at a factor $x = 54$. Fig. 9 compares the contact angles measured from 30 pL drops with the power law curves after scaling. The spreading speed is now in the correct time scale. Interestingly, the measured contact angles of the 30 pL drops are lower than expected at the beginning of the measurement. There are two potential reasons for this: the time resolution of 2000 s^{-1} is not good enough and/or the initial wetting is stronger because of the kinetic energy of the drop at the impact on the substrate. The kinetic energy of the drop is not considered in the model.

The main reason for the different spreading time scales between picoliter and microliter drops is their size difference. If we assume that the spreading speed is independent of the drop size like is predicted by the molecular kinetic model, the spreading time t_{spread} scales with the drop radius. The time it takes the drop to spread to a certain contact angle, can be calculated from the spreading speed v and the drop base radius r according to Eq. (15). If we compare drops of two different sizes the ratio of the times to spread to the same contact angle is given by the ratio of the radii, which scale relative to the cube root of the drop volume (Eq. (16)). The spreading time ratio of 3.5 μL and 30 pL drops is about 49 if a constant spreading speed is assumed which is close to the factor of 54 that was calculated from the measurements.

$$t_{spread} = \frac{r}{v} \tag{15}$$

$$\frac{t_{spread,3.5\mu L}}{t_{spread,30pL}} = \frac{r_{3.5\mu L} \cdot 1/v}{r_{30pL} \cdot 1/v} = \frac{V_{3.5\mu L}^{\frac{1}{3}}}{V_{30pL}^{\frac{1}{3}}} = 48.86 \tag{16}$$

2.4.5.2. Penetration. As observed during the validation of the combined LW-OWRK model, the penetration speeds predicted by the model were faster than measured values, but the trends were predicted well [37]. The reason for the deviation probably is that the LW equation describes a uniform flow in a cylindrical capillary while a number of pore sizes and geometries exist in paper which lead to a ragged liquid front and slower penetration speed. Therefore, the predicted penetration depths need to be slowed down. Again, we used the measurement of 30 pL drops as a reference. This time all model components (scaled spreading, evaporation, roughness, penetration) are used to calculate the drop volume of 30 pL drops over time. The scaling is done by multiplying the calculated penetration depth over time with a downscaling factor y. The measured and the modelled volume over time curves are compared and the scaling factor is chosen to minimize the deviation. Minimal error was achieved at $y = 0.046$. Fig. 10 compares the drop volume measured from 30 pL drops with the simulated volume curves after scaling of the penetration speed. The initially recorded drop volume of the measured drops is already considerably lower than 30 pL. This might again be related to the kinetic energy of the drop at impact causing faster wetting and faster absorption. However, Fig. 10 shows that the absorption speed should be in the correct time scale after scaling of the penetration speed.

3. Results after scaling

As all model components are now in the relevant time and size scales, the model can be used to predict the measured printed dot area. Since the shape of the printed dots deviates from a circle, the area equivalent diameter is used for comparison with model results. The issue of dot circularity is discussed in further detail in Section 6.1. For the industrial papers (Fig. 11 (a)) the general trends could be predicted with the model and a rather high R^2 of almost 0.7 could be achieved. For the lab papers (Fig. 11 (b)) the trends could be predicted well for medium to high surface tension liquids (TLC, TL3, TL4). The liquids with a low surface tension (TL1, TL2), however, do not follow the general trend which leads to the rather low R^2 of 0.37. Excluding TL1 and TL2, generates an R^2 of 0.86. The reason for the deviating behavior of the low surface tension liquids is not clear. One explanation could be that the drop area of the higher surface tension liquids is underestimated in the model because the kinetic energy driven spreading at the drop impact on the substrate is not considered. Shortly after the drop impact, the influence of the wettability on the spreading width is low (compare Zhang et al. [3]). The drops are forced into a flat shape independent of the contact angle. Thus, the kinetic energy will cause flatter drop shapes and bigger dots than predicted by the model especially for substrate-liquid pairings with low wettability. Another reason might be the dynamic contact angle curves being determined from μL drop data. For pL drops, the drop size is much smaller in relation to the roughness. For the low surface

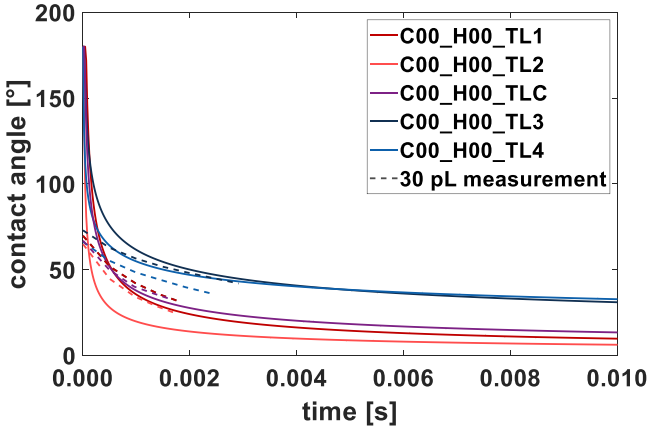

Fig. 9. Comparison of contact angles from 30 pL drops with predicted contact angles after scaling (scaling factor $x = 54$).

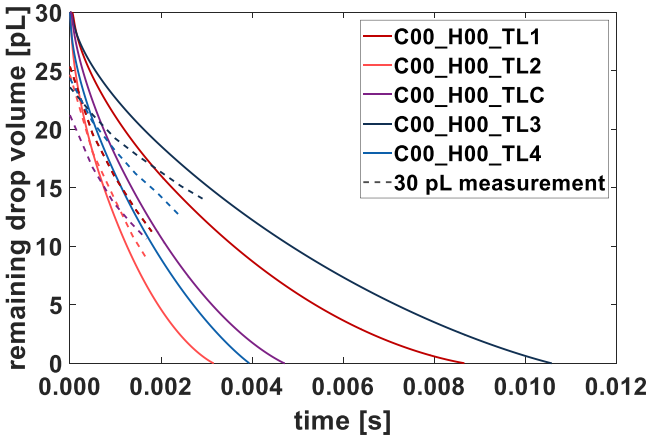

Fig. 10. Comparison of drop volume measured from 30 pL drops with predicted drop volume after scaling of penetration speed (scaling factor $y = 0.046$).

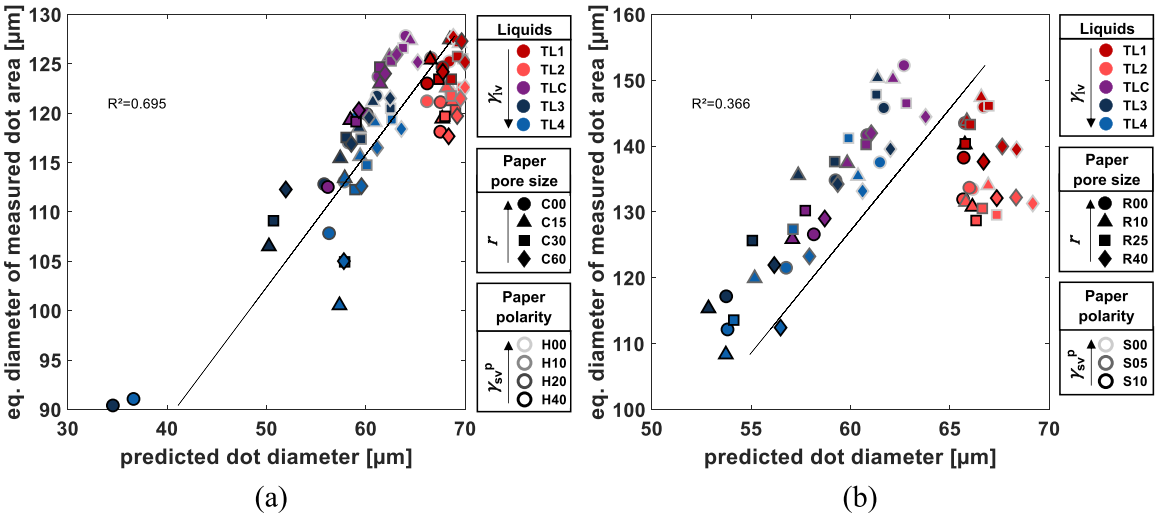

Fig. 11. Dot diameter predicted from the model vs. equivalent diameter of measured printed dot area. (a) industrial papers; (b) lab papers.

tension liquids which generally have a high wettability on all substrates, spreading might be inhibited more by the roughness. Indeed, there is less difference between the five test liquids in the measured 30 pL curves than in the predicted ones shown in Fig. 9. Furthermore, there are some indications that the dot size of the low surface tension liquids might be underestimated in the measurement due to the low color intensity of those prints in spite of all precautions taken to avoid this problem. This is further discussed in the limitations section.

Furthermore, the predicted dot diameters are significantly smaller than the measured ones. A reason for that could be the effect of optical dot gain. Based on the measurements of the light diffusion in paper (point spread function) by Praast et al. [45], the diffusion length of light in uncoated papers is in the range of 30–50 µm – large enough to explain at least part of the difference between modeled and measured dot size. It also needs to be considered that calendering and refining decreases the light scattering ability of the papers and thus increases the Yule-Nielsen effect. Accordingly, optical dot gain is expected to be stronger for calendered and refined papers.

4. Sensitivity analysis

Although the model components were either measured or corrected to fit the correct time scales, it is possible that a model component was under- or overestimated compared to the others. Furthermore, it is of interest if optima exist and if the addition of a model component increases the predictive power of the model at all. Therefore, a sensitivity analysis was performed. First, the equilibrium between spreading speed and penetration speed was investigated by a two-dimensional analysis. Next, the impact of roughness surface filling on the model fit was evaluated. Finally, the impact of up- or downscaling of the evaporation rates was studied.

4.1. Spreading speed vs. penetration speed

Fig. 12 shows the results of the sensitivity analysis for the combined effect of spreading speed and penetration speed. The data presented in Fig. 12 was produced by running the model many times with different overall penetration and spreading speeds which were independent of the scaling based on 30 pL measurements used before (Section 3). Different scaling factors x were used to change the spreading speed and scaling factors y to vary the penetration speed (x, y as defined in Section 2.4.5 prior to fitting to 30 pL measurements). The results based on scaling factors estimated from 30 pL measurements (Section 3) make up only a single data point in this diagram which is represented by a red marker. In the diagrams, the spreading speed is given as the decrease in contact angle per millisecond and calculated for the time it takes to reach the same contact angle as after 60 ms in the measurement of the microliter drops. The speed was calculated for each test point and the median speed of all test points was used for the x-axis of the diagram. Similarly, the penetration speed at a penetration depth of 1 µm was used to represent the penetration speed. Again, the median of all test points was used. Evaporation rates and volume reduction due to roughness were kept in the model unchanged. The R^2 was calculated for two scenarios: 1. the dot area is the result of the maximum extent of drop spreading and lateral liquid penetration further increases the dot area (scenario used in Section 3); 2. the dot area is the result of the maximum extent of drop spreading only, lateral penetration still decreases the drop volume.

Fig. 12 (a) shows the results for the industrial papers for the assumption that lateral penetration not only increases the liquid absorption but also the dot area at the surface. It shows that there is an optimum for penetration speed. Lower and higher than optimum penetration speeds result in a lower R^2. Especially too fast penetration speeds are harmful for the model fit. Also, too slow spreading, indicated by longer spreading times decreases the R^2. There however seems to be no upper limit for spreading speed. A reason could be that spreading is accelerated due to the kinetic energy available at the drop impact on the surface. The model prediction presented in Section 3 (red marker) is close to the area of maximum R^2 which indicates that the scaling with 30 pL measurements was a good estimate. Fig. 12 (b) shows the results for the industrial papers if the dot area is calculated as the maximum base diameter of the liquid drop above the surface and the area is not increased by lateral penetration. Overall, the results are similar as in Fig. 12 (a) but a bit lower R^2 is achieved. Also, lower than optimum penetration speeds have only a minor impact on the R^2 if lateral penetration is not assumed to increase the dot area.

The results for the lab papers are shown in Fig. 12 (c) and (d). Fig. 12 (c) shows the results for the assumption that the dot area is increased by lateral spreading. The results are very similar as if lateral penetration is not considered to increase the dot area (Fig. 12 (d)). The optimum penetration speeds are generally lower than for the industrial papers and there is hardly a lower limit discernable. This however might be related to TL1 and TL2 not fitting the general trend. If these two liquids are excluded from the evaluation, the results are more similar to the industrial papers' results and the penetration speed optimum is at the same order of magnitude (graphs for evaluation without TL1 and TL2 can be found in the ESI).

All in all, the impact of the penetration seems to be minor as long as the penetration speed is not overestimated as indicated by the rather

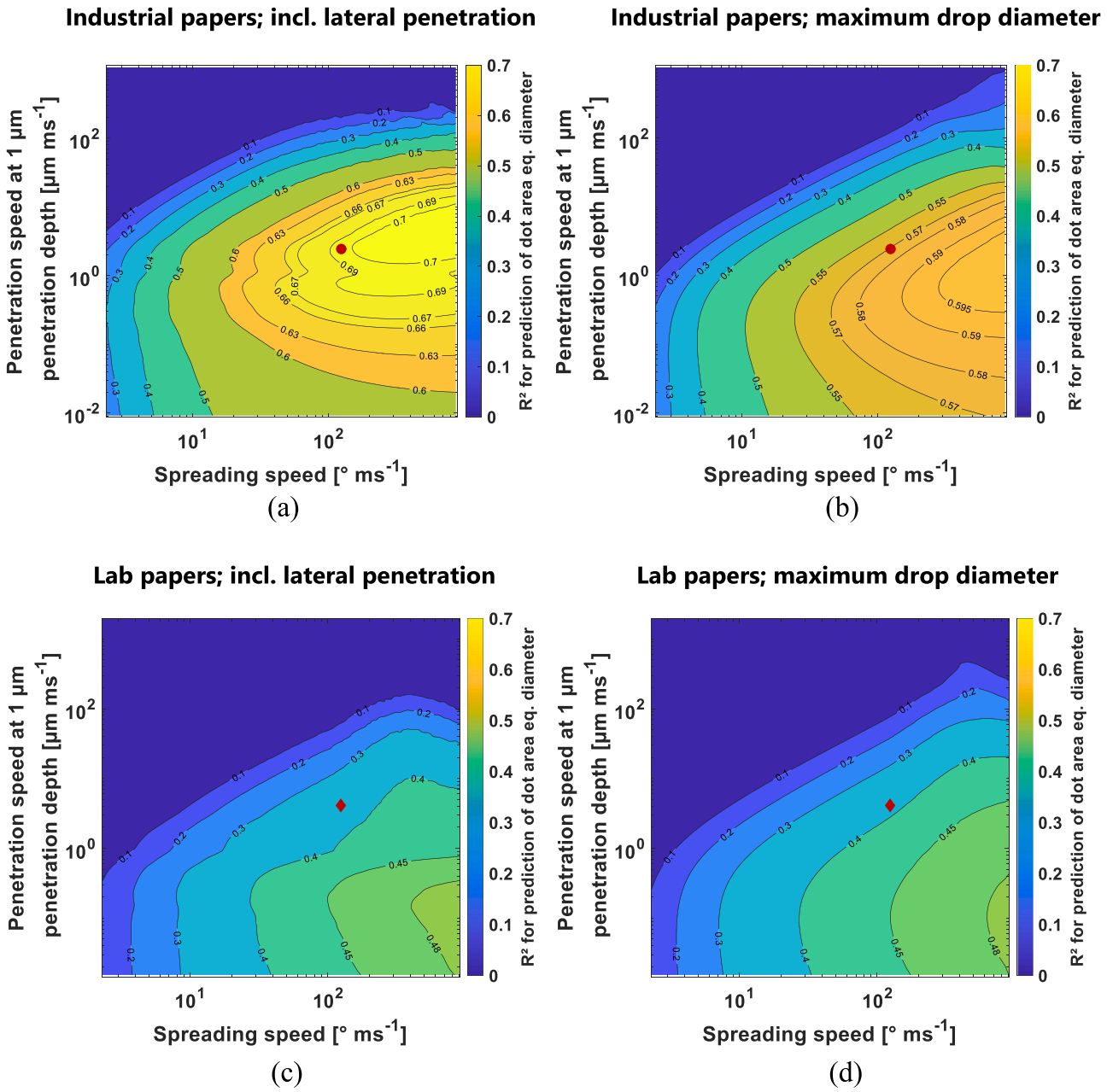

Fig. 12. Sensitivity analysis for the combined effect of penetration speed and spreading speed on model fit: (a) industrial papers – lateral penetration increases dot area; (b) industrial papers – lateral penetration reduces drop volume but does not increase dot area. Dot area is calculated as the maximum diameter of the drop on the surface; (c) lab papers – lateral penetration increases dot area; (d) lab papers – lateral penetration reduces drop volume but does not increase dot area. There seems to be an optimum for penetration speed while R^2 is highest at the highest spreading speeds. Red markers represent the model results after scaling presented in Section 3.

high R^2 at very low penetration speeds. Also including lateral penetration in the area calculation can improve the model only to a minor extent. The results of this analysis suggest that the dot spreading is very fast and it is a much more important factor determining the final dot area than liquid penetration. This is further corroborated by additional data presented in Section 5.

4.2. *Impact of roughness surface filling*

The impact of including surface roughness filling into the model is evaluated for different size scales in Fig. 13. All other model components were kept constant as in Section 3. The roughness was set to zero as a starting point. Then roughness in terms of void volume of the surface was increased by using different threshold wavelengths in the FFT filtering. A higher filter wavelength leads to a higher roughness value. Fig. 13 shows that including roughness into the model at a low filter wavelength slightly improved the fit. At higher filter wavelengths the roughness impact is overestimated and thus leads to a poorer fit. This is plausible because the measured dot sizes are in the range of 90–150 µm. Irregularities bigger than 150 µm thus can hardly affect the drops. The trend is the same for industrial and lab papers, although the differences are less for the lab papers. This is not surprising because of the generally lower R^2 of the lab papers.

Overall, the roughness impact in terms of drop volume reduction seems to be low. However, it should not be forgotten that roughness also influences the spreading which is not considered in this analysis. The

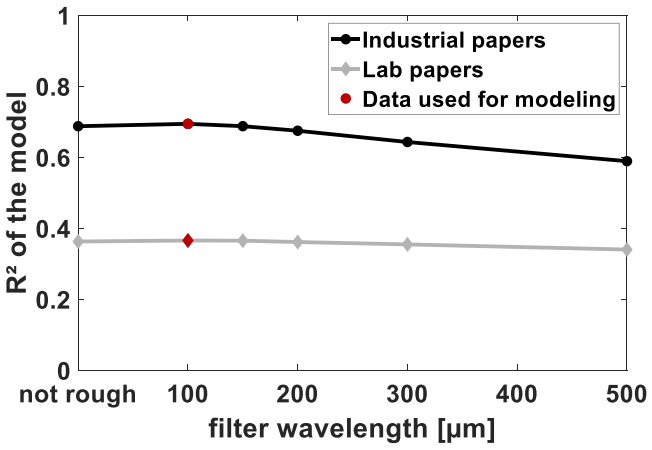

Fig. 13. Impact of including surface roughness filling into the model and of different filter wavelengths used to calculate the void volume of the surface. A higher filter wavelength leads to higher void volumes and thus a bigger roughness impact in the model. Including roughness filling into the model slightly improves the R^2 while higher filter wavelengths cause an overestimation of the effect and a lower R^2. The red markers indicate values used in the model presented in Section 3.

roughness impact on spreading is already contained in the contact angle data used to simulate the spreading behavior and thus cannot be analyzed separately. Furthermore, another reason for the low impact of roughness filling might be related to the fact that roughness and pore sizes of the substrates could not be varied independently. Both calendering and refining not only decreased the pore sizes but also the roughness. This might explain why adding roughness filling to a model that already considers the penetration speed (and the related impact of pore size) did not result in a significant improvement of the model predictive power.

4.3. Impact of evaporation rate

The impact of including evaporation into the model is evaluated in Fig. 14. The evaporation rate first was set to zero. Then the measured evaporation rates (red markers) were multiplied by a factor to increase or decrease the impact of evaporation in the model. All other model components were kept constant as in Section 3. Including evaporation into the model slightly improved the model fit for the lab papers only.

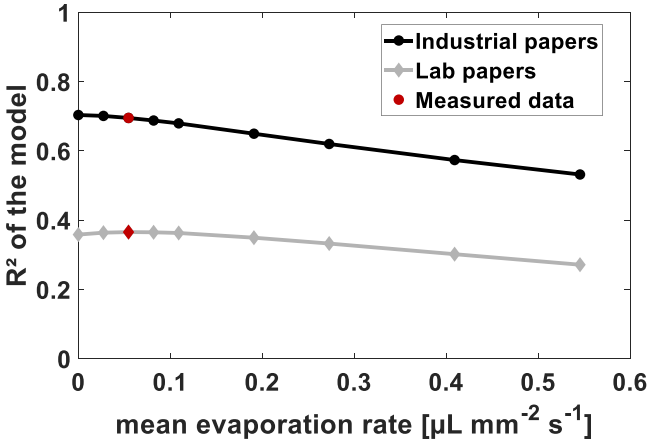

Fig. 14. Impact of including evaporation into the model on model quality. The red markers indicate the measured evaporation rates which were multiplied by a factor for the other evaluated scenarios. Including evaporation slightly improved the model fit for the lab papers only. Higher evaporation rates affected the model fit negatively.

Further increasing the evaporation rates had a negative effect on model fit. Overall, evaporation seems to have a negligible effect on the printed dot area, which is plausible as it is much slower than absorption into the substrate. This is also in line with Tan [10] arguing that evaporation happens at a much longer time scale than the other processes.

4.4. Conclusions on sensitivity analysis

All in all, the sensitivity analysis suggests that spreading in terms of wettability is the dominant mechanism determining the dot area. Highest R^2s were obtained at very high spreading speeds which means that the dynamic part of the spreading is rather irrelevant for the final dot area as it is not the limiting factor. The reason for that could be that the spreading is accelerated due to the kinetic energy available at the drop impact on the surface. Penetration has a low impact on the resulting model fit over a large range of penetration speeds. Between a y-axis range of 10^{-2} and 10^{2} µm ms^{-1} for penetration speed in Fig. 12 the correlation is quite good, indicating that it does not matter too much, as long as it is not too fast. It needs to be pointed out, however, that this result is obtained looking at test points that cover a wide range of penetration speeds within each data set. For the test points with high absorption speeds, absorption might still play a significant role in limiting the extent of drop spreading. Surface roughness filling and evaporation seem to be rather irrelevant as they only have a minor impact on the model fit.

5. Consequences – empirical results

The findings of the sensitivity analysis have several implications. As shown, the model quality is mainly affected by the balance between spreading and absorption. Accordingly, the properties which affect spreading and absorption most can be used for an empirical analysis of the printed dot data. The contact angle between the liquid and the substrate describes the wettability and at the same time influences the absorption speed. Fig. 15 shows that the printed dot area is highly correlated with the contact angle for both industrial and lab papers. Only the test liquid.

TL2 does not follow the general trend. An explanation is that the extremely fast absorption of this test liquid limits the extent of spreading and therefore the dot area is smaller than expected due to the wettability. For higher contact angles, the dot area decreases, which indicates that the wettability and the related extent of spreading is the determining factor for all other liquids besides TL2. If the impact of the wettability on the penetration speed was dominant, higher contact angles would lead to bigger dots as the penetration speeds are lower and there is more time for spreading. The rather high predictive power of the contact angle is in line with earlier findings where contact angles from microliter drops were well correlated with inkjet printed picoliter dot area of different liquids and substrates [44].

Besides the contact angle, also the base diameter detected in the contact angle measurements can be used as an estimate for the printed dot area. The maximum detected drop base diameter of the measured µL drops is a result of spreading and simultaneous absorption. The same is true for the printed pL dots. Even though the printed drops are much smaller, the maximum base diameter of the µL drops is an even better predictor than the contact angle (compare Fig. 15 (c) and (d)). This is a further indication that the wettability is the most important factor determining the dot area as penetration of the pL drops is much faster than of the µL drops. The overall wettability, however, is independent of the drop size.

Similar high R^2s as with the maximum base diameter can be obtained if the liquid viscosity is considered in addition to the contact angle. Besides the contact angle, also the liquid viscosity has an impact on both spreading and absorption. In a multiple linear regression model including the contact angle and the viscosity, both terms are significant (model fit is shown in Fig. 16). For both data sets, a higher viscosity is

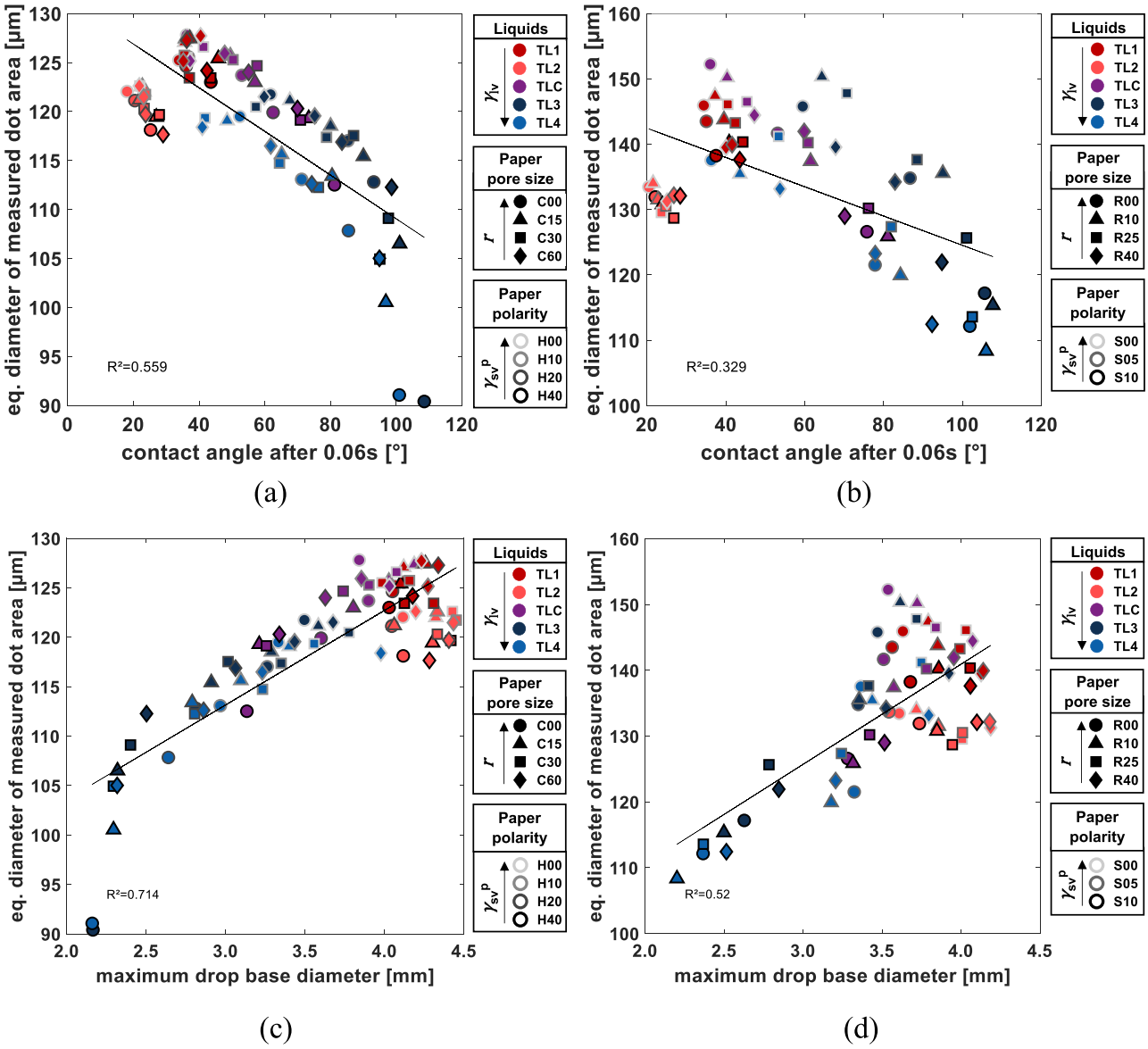

Fig. 15. Top row: Contact angles after 60 ms vs. equivalent diameter of printed dot area: (a) industrial papers; (b) lab papers. Printed dot area is strongly correlated with the contact angle except for TL2. Bottom row: Maximum detected drop base diameter vs. equivalent diameter of printed dot area: (c) industrial papers; (d) lab papers. Correlation of the maximum detected drop base diameter is even slightly better than correlation with the contact angle.

related to bigger dots. Accordingly, the impact of the viscosity on the penetration speed seems to be the dominant effect. As the viscosity slows down the absorption, more time is available for spreading and lateral penetration which increases the dot area. At the same time the viscosity also slows down the spreading, which seemingly has less effect than the slowed down absorption.

6. Limitations

Although the model could predict the printed dot area to a certain extent, there are some limitations that reduce its predictive power. As explained before, the dot area of higher surface tension liquids might be underestimated in the model because the kinetic energy driven spreading immediately after the drop impact is not considered.

Furthermore, it needs to be considered that only uncoated paper substrates were studied in this work. The liquid absorption in coated paper substrates, however, might not be described accurately enough with the Lucas-Washburn equation. The pore lengths in a porous coating are short. Thus, the liquid front encounters a series of accelerations and decelerations caused by the frequently changing pore diameters and inertia consequently has a significant impact on liquid absorption in coated papers [32]. Also, the much higher amount of very fine pores might cause different absorption behaviors than observed for the studied uncoated papers (compare e.g. [30,46]). Therefore, the results of this study might not be directly transferable to coated papers and it would be interesting to perform a similar study with coated papers.

Beyond that the issue of dot circularity and dot color intensity needs to be discussed in more detail.

6.1. Dot circularity

The drops are simulated as the cap of a sphere in the model and thus also the finally predicted dot is circular. In reality, the shapes of the printed dots can deviate strongly from a circle. How strongly the drop shapes deviate from a circular shape mainly depends on the wettability as shown in Fig. 17 for the industrial papers. The higher the contact angle, the more elongated the dot shape gets which is shown by the increasing aspect ratio. At low contact angles, the liquid can spread more

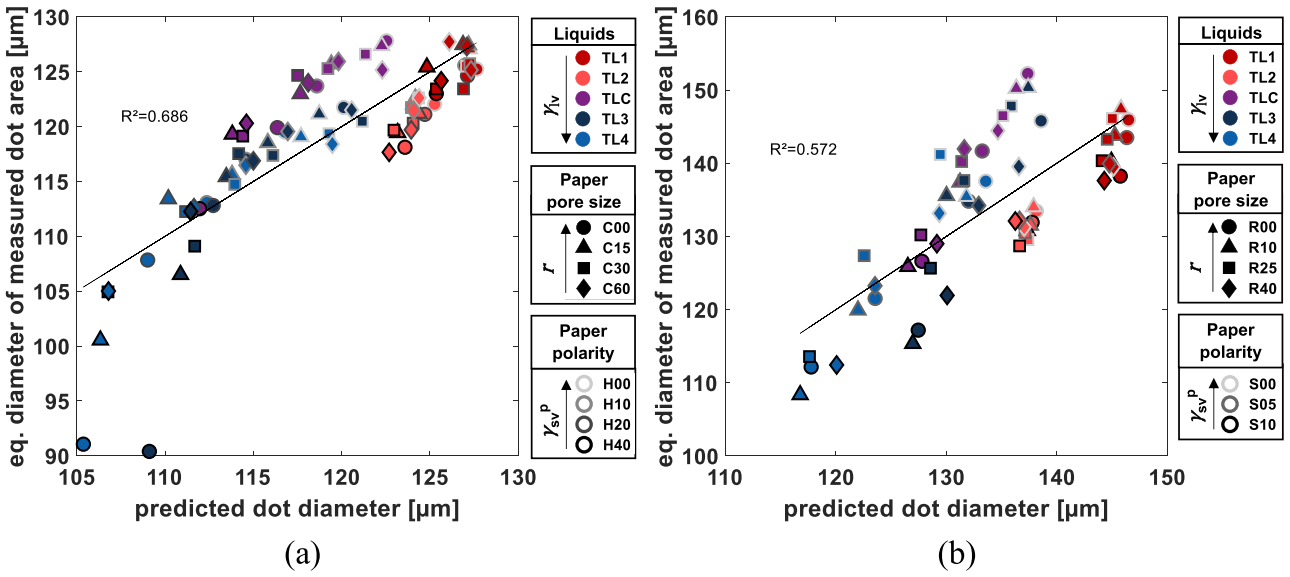

Fig. 16. Multiple linear regression model using the contact angle and liquid viscosity as predictors for the prediction of dot area equivalent diameter: (a) industrial papers; (b) lab papers. The contact angle is inversely proportional to the dot diameter, while a higher viscosity is related to bigger dots.

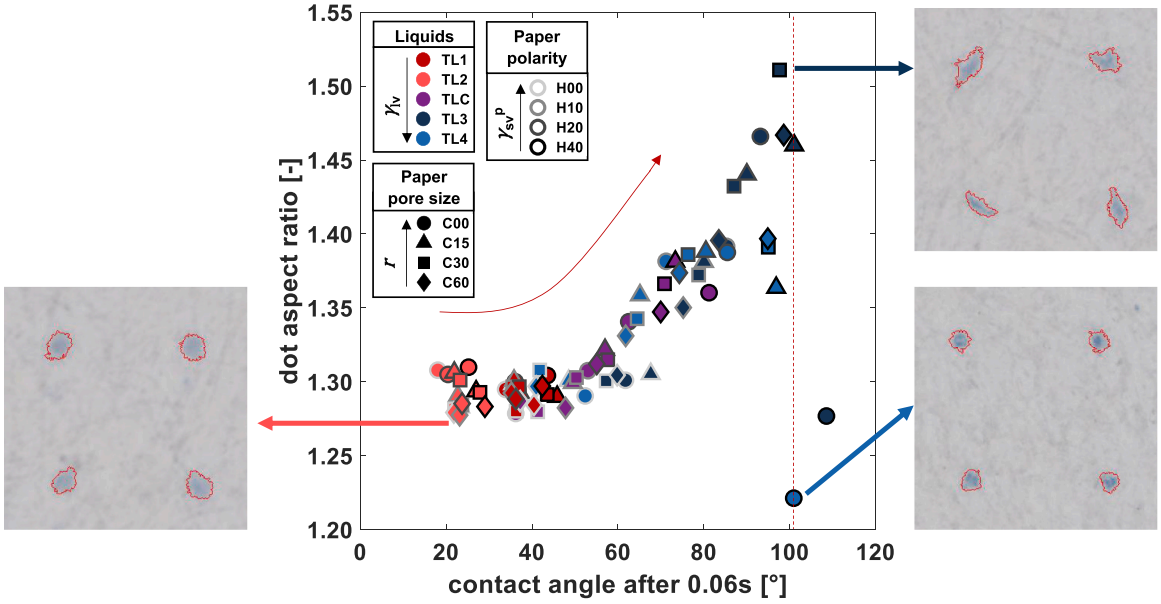

Fig. 17. Dependence of the dot aspect ratio on the wettability (contact angle) for the industrial papers. At higher contact angles the dot shapes are more irregular indicated by a higher aspect ratio caused by preferential spreading along the fibers. An extremely low wettability results in smaller dots with a low aspect ratio as spreading is completely inhibited.

or less freely in all directions. At higher contact angles, spreading is partially hindered. These observations are in line with findings of Ezzatneshan et al. [21] who observed that the wetted area was more roundish for a lower contact angle. At very high contact angles, however, spreading is inhibited in all directions resulting also in round but small dots. The elongated dot shapes can be attributed to preferential spreading along the fibers [21]. This is in line with the orientation of the dots strongly resembling the anisotropic fiber orientation of the industrially produced paper sheet (diagram in the ESI).

Another interesting aspect of dot circularity is shown in Fig. 18: after fitting an ellipse to the dot area, the wettability mainly affects the size of the dot ellipse minor axis while the dot major axis is almost unaffected over a wide range of contact angles. Since the elliptical shape of the dots is caused by preferential spreading along the fibers, the major axis will be in fiber direction in most cases. Fig. 18 suggests that for good wetting dot spreading is independent of surface topography, but when the wetting decreases, topography starts to play a role as the dots are spreading more along the fibers than across them.

The trend of higher aspect ratios at higher contact angles is the same for the lab papers but at a higher degree of scattering. The fiber orientation of lab sheets is isotropic. As expected also the printed dots are oriented randomly in all directions. The effect of the wettability on minor and major dot axis for the lab papers is similar as for the industrial papers even if the trend is less pronounced due to the larger degree of scattering (all diagrams for the lab papers can be found in the ESI).

The oval shape of the dots complicates the predictability of the dot area. Accordingly, the R^2 increases if the measured dot area is corrected by the aspect ratio for all fits, no matter if the model or the empirical

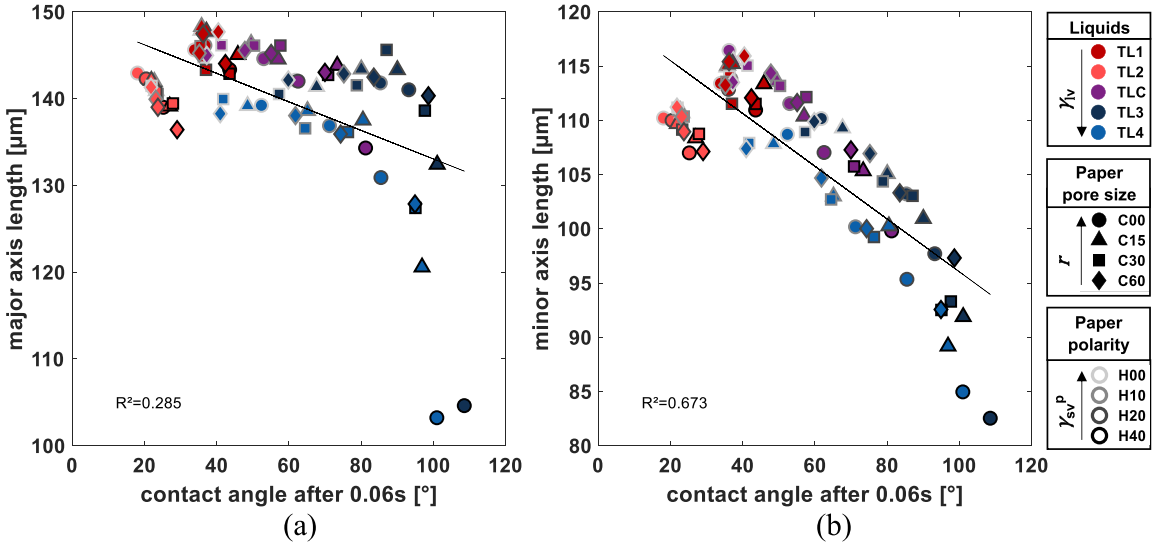

Fig. 18. Influence of the wettability on (a) major axis length or (b) minor axis length of the printed dots on the industrial papers. Wettability mainly affects the minor axis length while the major axis length changes little over a wide range of contact angles.

relations are used (results in the ESI).

6.2. Color intensity

The dots need to be clearly distinguishable from the background to guarantee a good dot detection. However, there is no clear cutoff between dot and background. Rather there is a color gradient from the drop center to the edge. Moreover, the color intensity varies for different substrate-liquid pairings. The bigger the dot area the less contrast have the dots. If a constant threshold is used for the binarization, the size of the bigger, brighter dots will be underestimated because of the low color intensity. In the image analysis this problem was reduced by amplifying the gray scale image before the binarization (i.e. increasing the contrast, compare Fig. 4(b)). It cannot be completely avoided, however. An alternative way to estimate the dot area is to use the light absorption calculated from squares and divide it by the color intensity of the dot. As expected, the detected dot area correlates strongly with this area estimate. However, the dots of TL1 and TL2 are estimated to be bigger if the light absorption is used for the area estimation. This might be an indication that the dot area of TL1 and TL2 is underestimated in the detection which is plausible because of the low color intensity of those dots. Moreover, the R^2 increases for the model as well as empirical fits if the area estimated from light absorption is used, especially for the lab papers. Combining the area estimated from light absorption with the aspect ratio correction further increases the R^2 resulting in a R^2 of 0.80 for the industrial papers and of 0.59 for the lab papers. A more thorough discussion and result diagrams can be found in the ESI.

7. Conclusions

The area of inkjet printed picoliter dots is the result of several processes taking place simultaneously: drop spreading, absorption and evaporation. In experimental studies dealing with the evolution of a drop on a porous substrate (e.g. [2,6,9–16,28]) generally only a low number of liquids and/or substrates is studied. The aim of this work was to first explain experimental results of inkjet dot area by a simple model describing the most important physical parameters (penetration, spreading, evaporation, roughness). Second, we quantitatively analyzed the relevance of these parameters for a range of uncoated paper substrates (with varying polarity and porosity) and liquids (with varying viscosity and surface tension).

The printed dot area could be predicted reasonably well with a simple model including liquid spreading, absorption and evaporation as well as volume reduction due to surface roughness filling. A sensitivity analysis showed that the most important factor is the spreading behavior in terms of wettability, followed by penetration. The evaporation effect is negligible probably because it is too slow to significantly affect the extent of dot spreading. Including volume reduction due to surface roughness filling also had only a minor impact on the model.

These findings were in line with empirical results showing a high correlation of the liquid-substrate contact angle and the viscosity with the dot area. Especially the contact angle and the maximum drop base diameter had a high predictive power and the spreading was also the most important factor in the sensitivity analysis. Moreover, it needs to be considered that the dot shapes get more elongated and irregular at higher contact angles, except if the wettability is very low. The dot orientation follows the fiber orientation. The major axis of the dot which is aligned in the direction of the fibers is less affected by the wettability than the dot spreading in the perpendicular direction. We conclude that surface topography does not play a role for dot spreading of well wetting liquids, but becomes increasingly relevant for liquids that are not wetting the surface well. For future work, it would be interesting to perform a similar study on coated papers.

CRediT authorship contribution statement

Carina Waldner: Conceptualization, Methodology, Data curation, Validation, Formal analysis, Investigation, Writing – original draft, Writing – review & editing, Visualization. **Alfons Ritzer:** Validation, Investigation, Resources. **Ulrich Hirn**: Conceptualization, Methodology, Writing – original draft, Writing – review & editing, Supervision, Project administration, Funding acquisition.

Declaration of Competing Interest

The authors declare that they have no known competing financial interests or personal relationships that could have appeared to influence the work reported in this paper.

Data Availability

Data will be made available on request.

Acknowledgement

The financial support by the Austrian Federal Ministry for Digital and Economic Affairs and the National Foundation for Research Technology and Development is gratefully acknowledged. We also thank our industrial partners Mondi, Canon Production Printing, Kelheim Fibres, and SIG Combibloc for their financial support.

Appendix A. Supporting information

Supplementary data associated with this article can be found in the online version at doi:10.1016/j.colsurfa.2023.131986.

References

[1] H. Deng, Y. Huang, Y. Yang, S. Wu, Z. Chen, Three-dimensional numerical investigation on micro-meter droplet impact and penetration into the porous media with different velocities, MATEC Web Conf. 355 (2022) 01009, https://doi.org/10.1051/matecconf/202235501009.
[2] S.M. Kumar, A.P. Deshpande, Dynamics of drop spreading on fibrous porous media, Colloids Surf. A Physicochem. Eng. Asp. 277 (2006) 157–163, https://doi.org/10.1016/j.colsurfa.2005.11.056.
[3] L. Zhang, L. Liu, J. Chen, Z. Jin, P. Li, Impact and penetration dynamics of inkjet droplet within paper-like fibrous substrate by mesoscopic modeling, Comput. Mech. 66 (2020) 391–404, https://doi.org/10.1007/s00466-020-01856-8.
[4] G. Zhang, M.A. Quetzeri-Santiago, C.A. Stone, L. Botto, J.R. Castrejón-Pita, Droplet impact dynamics on textiles, Soft Matter 14 (2018) 8182–8190, https://doi.org/10.1039/C8SM01082J.
[5] S. Krainer, C. Smit, U. Hirn, The effect of viscosity and surface tension on inkjet printed picoliter dots, RSC Adv. 9 (2019) 31708–31719, https://doi.org/10.1039/c9ra04993b.
[6] G. Desie, G. Deroover, F. De Voeght, A. Soucemarianadin, Printing of dye and pigment-based aqueous inks onto porous substrates, J. Imaging Sci. Technol. 48 (2004) 389–397, https://doi.org/10.2352/J.ImagingSci.Technol.2004.48.5.art00005.
[7] A. Lundberg, J.Ö. Örtegren, E. Alfthan, G. Ström, Paper-ink interactions: microscale droplet absorption into paper for inkjet printing, Nord. Pulp Pap. Res. J. 26 (2011) 142–150, https://doi.org/10.3183/npprj-2011-26-01-p142-150.
[8] G. Venditti, V. Murali, A.A. Darhuber, Inkjet printing of surfactant solutions onto thin moving porous media, Colloids Surf. A Physicochem. Eng. Asp. 634 (2022), 127832, https://doi.org/10.1016/j.colsurfa.2021.127832.
[9] M. Denesuk, G.L. Smith, B.J.J. Zelinski, N.J. Kreidl, D.R. Uhlmann, Capillary Penetration of Liquid Droplets into Porous Materials, Academic Press, 1993, https://doi.org/10.1006/jcis.1993.1235.
[10] H. Tan, Absorption of picoliter droplets by thin porous substrates, AIChE J. 63 (2017) 1690–1703, https://doi.org/10.1002/aic.15525.
[11] R.K. Holman, M.J. Cima, S.A. Uhland, E. Sachs, Spreading and infiltration of inkjet-printed polymer solution droplets on a porous substrate, J. Colloid Interface Sci. 249 (2002) 432–440, https://doi.org/10.1006/jcis.2002.8225.
[12] A. Clarke, T.D. Blake, K. Carruthers, A. Woodward, Spreading and imbibition of liquid droplets on porous surfaces, Langmuir 18 (2002) 2980–2984, https://doi.org/10.1021/la0117810.
[13] V.M. Starov, S.R. Kostvintsev, V.D. Sobolev, M.G. Velarde, S.A. Zhdanov, Spreading of liquid drops over dry porous layers: complete wetting case, J. Colloid Interface Sci. 252 (2002) 397–408, https://doi.org/10.1006/jcis.2002.8450.
[14] R.C. Daniel, J.C. Berg, Spreading on and penetration into thin, permeable print media: application to ink-jet printing, Adv. Colloid Interface Sci. 126 (2006) 439–469, https://doi.org/10.1016/j.cis.2006.05.012.
[15] K.L. Yip, A.R. Lubinsky, D.R. Perchak, K.C. Ng, Measurement and modeling of drop absorption time for various ink-receiver systems, J. Imaging Sci. Technol. 47 (2003) 388–393, https://doi.org/10.2352/J.ImagingSci.Technol.2003.47.5.art00004.
[16] H. Modaressi, G. Garnier, Mechanism of wetting and absorption of water droplets on sized paper: Effects of chemical and physical heterogeneity, Langmuir 18 (2002) 642–649, https://doi.org/10.1021/la0104931.
[17] D. Seveno, V. Ledauphin, G. Martic, M. Voué, J. De Coninck, Spreading drop dynamics on porous surfaces, Langmuir 18 (2002) 7496–7502, https://doi.org/10.1021/la025520h.
[18] S.H. Davis, L.M. Hocking, Spreading and imbibition of viscous liquid on a porous base, Phys. Fluids 11 (1999) 48–57, https://doi.org/10.1063/1.869901.
[19] S.H. Davis, L.M. Hocking, Spreading and imbibition of viscous liquid on a porous base. II, Phys. Fluids 12 (2000) 1646–1655, https://doi.org/10.1063/1.870416.
[20] R.T. van Gaalen, C. Diddens, D.P. Siregar, H.M.A. Wijshoff, J.G.M. Kuerten, Absorption of surfactant-laden droplets into porous media: a numerical study, J. Colloid Interface Sci. 597 (2021) 149–159, https://doi.org/10.1016/j.jcis.2021.03.119.
[21] E. Ezzatneshan, R. Goharimehr, Study of spontaneous mobility and imbibition of a liquid droplet in contact with fibrous porous media considering wettability effects, Phys. Fluids 32 (2020), https://doi.org/10.1063/5.0027960.
[22] X. Frank, P. Perré, Droplet spreading on a porous surface: a lattice Boltzmann study, Phys. Fluids 24 (2012), https://doi.org/10.1063/1.3701996.
[23] F. Fu, P. Li, K. Wang, R. Wu, Numerical simulation of sessile droplet spreading and penetration on porous substrates, Langmuir 35 (2019) 2917–2924, https://doi.org/10.1021/acs.langmuir.8b03472.
[24] N.C. Reis, R.F. Griffiths, J.M. Santos, Numerical simulation of the impact of liquid droplets on porous surfaces, J. Comput. Phys. 198 (2004) 747–770, https://doi.org/10.1016/j.jcp.2004.01.024.
[25] N.C. Reis, R.F. Griffiths, J.M. Santos, Parametric study of liquid droplets impinging on porous surfaces, Appl. Math. Model. 32 (2008) 341–361, https://doi.org/10.1016/j.apm.2006.12.006.
[26] P. Alam, M. Toivakka, K. Backfolk, P. Sirviö, Impact spreading and absorption of Newtonian droplets on topographically irregular porous materials, Chem. Eng. Sci. 62 (2007) 3142–3158, https://doi.org/10.1016/j.ces.2007.03.018.
[27] N. Alleborn, H. Raszillier, Spreading and sorption of a droplet on a porous substrate, Chem. Eng. Sci. 59 (2004) 2071–2088, https://doi.org/10.1016/j.ces.2004.02.006.
[28] H. Aslannejad, H. Fathi, S.M. Hassanizadeh, A. Raoof, N. Tomozeiu, Movement of a liquid droplet within a fibrous layer: direct pore-scale modeling and experimental observations, Chem. Eng. Sci. 191 (2018) 78–86, https://doi.org/10.1016/j.ces.2018.06.054.
[29] M. Choi, G. Son, W. Shim, A level-set method for droplet impact and penetration into a porous medium, Comput. Fluids 145 (2017) 153–166, https://doi.org/10.1016/j.compfluid.2016.12.014.
[30] C.J. Ridgway, P.A.C. Gane, J. Schoelkopf, Modified calcium carbonate coatings with rapid absorption and extensive liquid uptake capacity, Colloids Surf. A Physicochem. Eng. Asp. 236 (2004) 91–102, https://doi.org/10.1016/j.colsurfa.2003.12.030.
[31] M. Liu, J. Wu, Y. Gan, D.A.H. Hanaor, C.Q. Chen, Evaporation limited radial capillary penetration in porous media, Langmuir 32 (2016) 9899–9904, https://doi.org/10.1021/acs.langmuir.6b02404.
[32] J. Schoelkopf, P.A.C. Gane, C.J. Ridgway, G.P. Matthews, Influence of inertia on liquid absorption into paper coating structures, Nord. Pulp Pap. Res. J. 15 (2000) 422–430, https://doi.org/10.3183/npprj-2000-15-05-p422-430.
[33] G.H. McKinley, M. Renardy, Wolfgang von Ohnesorge, Phys. Fluids 23 (2011), https://doi.org/10.1063/1.3663616.
[34] D.K. Owens, R.C. Wendt, Estimation of the surface free energy of polymers, J. Appl. Polym. Sci. 13 (1969) 1741–1747, https://doi.org/10.1002/app.1969.070130815.
[35] W. Rabel, Einige Aspekte der Benetzungstheorie, und ihre Anwendung auf die Untersuchung und Veränderung der Oberflächeneigenschaften von Polymeren, Farbe Und Lack. 77 (1971).
[36] D.H. Kaelble, Dispersion-polar surface tension properties of organic solids, J. Adhes. 2 (1970) 66–81, https://doi.org/10.1080/0021846708544582.
[37] C. Waldner, U. Hirn, Modeling liquid penetration into porous materials based on substrate and liquid surface energies, J. Colloid Interface Sci. 640 (2023) 445–455, https://doi.org/10.1016/j.jcis.2023.02.116.
[38] C. Waldner, A. Mayrhofer, U. Hirn, Measuring liquid penetration in thin, porous sheets with ultrasound and drop absorption – scope and limitations, Colloids Surf. A Physicochem. Eng. Asp. 650 (2022), 129551, https://doi.org/10.1016/j.colsurfa.2022.129551.
[39] P. Wulz, C. Waldner, S. Krainer, E. Kontturi, U. Hirn, S. Spirk, Surface hydrophobization of pulp fibers in paper sheets via gas phase reactions, Int. J. Biol. Macromol. 180 (2021) 80–87, https://doi.org/10.1016/j.ijbiomac.2021.03.049.
[40] A. Oko, P.M. Claesson, P. Niga, A. Swerin, Measurements and dimensional scaling of spontaneous imbibition of inkjet droplets on paper, Nord. Pulp Pap. Res. J. 31 (2016) 156–169, https://doi.org/10.3183/npprj-2016-31-01-p156-169.
[41] R. Lucas, Über das Zeitgesetz, des kapillaren Aufstiegs von Flüssigkeiten, Kolloid-Z. 23 (1918) 15–22, https://doi.org/10.1007/BF01461107.
[42] E.W. Washburn, The dynamics of capillary flow, Phys. Rev. 17 (1921) 273–283, https://doi.org/10.1103/PhysRev.17.273.
[43] J. Järnström, M. Järn, C.M. Tåg, J. Peltonen, J.B. Rosenholm, Liquid spreading on ink-jet paper evaluated by the hydrodynamic and molecular-kinetic models, J. Adhes. Sci. Technol. 25 (2011) 761–779, https://doi.org/10.1163/016942410×525993.
[44] S. Krainer, L. Saes, U. Hirn, Predicting inkjet dot spreading and print through from liquid penetration- and picoliter contact angle measurement, Nord. Pulp Pap. Res. J. 35 (2020) 124–136, https://doi.org/10.1515/npprj-2019-0088.
[45] H. Praast, T. Ziegenbein, L. Göttsching, Der Einfluss von Lichtfang und Druckübertragungsprozess auf die Druckqualität. Teil I, Int. Pap. 5 (2003) T68–T73.
[46] C.J. Ridgway, P.A.C. Gane, Controlling the absorption dynamic of water-based ink into porous pigmented coating structures to enhance print performance, Nord. Pulp Pap. Res. J. 17 (2002) 119–129, https://doi.org/10.3183/npprj-2002-17-02-p119-129.